Journal of Solid State Chemistry **145,** 37–49 (1999)
Article ID jssc.1999.8198, available online at http://www.idealibrary.com on IDEAL®

An Electron and X-Ray Powder Diffraction Study of the Defect Fluorite Structure of $Mn_{0.6}Ta_{0.4}O_{1.65}$

S. Esmaeilzadeh, J. Grins,[1] and A.-K. Larsson

Department of Inorganic Chemistry, Arrhenius Laboratory, Stockholm University, SE-106 91 Stockholm, Sweden

Received September 24, 1998; in revised form January 28, 1999; accepted February 7, 1999

The oxide $Mn_{0.6}Ta_{0.4}O_{1.65}$ has been synthesized in air by rapidly cooling a melt from 1400°C, and it has been studied by X-ray powder diffraction (XRPD), selected-area electron diffraction (SAED), high-resolution electron microscopy (HREM), thermal analysis, and measurements of magnetic susceptibility and electrical conductivity. The average structure is that of a cubic fluorite with $a = 4.9826(3)$ Å and 18% vacancies on the O atom sites. Prominent diffuse scattering is present in its electron diffraction patterns (EDP's) and a structural model for this scattering is proposed. It is based on ca. 10 Å large microdomains with a pyrochlore type structure which are separated by antiphase boundaries. The magnetic susceptibility shows an antiferromagnetic interaction between the Mn^{2+} ions and an effective number of Bohr magnetons that increases with temperature. When heated in air at 500°C, the compound is oxidized to the composition $Mn_{0.6}Ta_{0.4}O_{1.75}$, while retaining a cubic fluorite structure with $a = 4.8380(4)$ Å. This latter phase is a semiconductor with an activation energy of 0.64 eV. © 1999 Academic Press

INTRODUCTION

Our initial interest in Mn–Ta oxides was in synthesizing a series of known phases in order to use them as precursors for the synthesis of new oxynitrides containing Mn and Ta (1). Since the crystal structures of several reported phases had not been determined, structural studies of these were initiated.

Turnock (2) studied the phase relations in the Mn–Ta–O system at 1200°C and partial pressures of oxygen (pO_2) between 10^{-17} and 1 atm. Four Mn–Ta oxides were observed at $pO_2 = 10^{-17}$ atm, all containing Mn in an oxidation state of +2: $MnTa_2O_6$ with the orthorhombic columbite-type structure (3), $Mn_4Ta_2O_9$ with a corundum-related structure (4), and two phases, $Mn_{1.4}TaO_{3.9}$ and $Mn_6Ta_2O_{11}$, with structures unknown at that time. In addition, two oxides containing Mn^{3+} were obtained at $pO_2 = 1$ atm: $MnTaO_4$, stable only below 1000°C, and $Mn_{1.4}TaO_{4.2}$, both with undetermined crystal structures. Mn–Ta oxides with metallic character and very low oxidation states of Ta have been reported by Schönberg (5): Mn_3Ta_3O with an η-carbide structure, and Mn_2TaO_3 with a structure related to that of CoSn (B35 type).

The phase designated as $Mn_6Ta_2O_{11}$ by Turnock (2) has subsequently been shown to have the composition $Mn_{11}Ta_4O_{21}$ (6). It has a trigonal structure with $a = 5.3776(2)$, $c = 34.040(2)$ Å that contains $Mn_4Ta_2O_9$ corundum-type blocks alternating with single MnO layers of octahedra. We have recently determined the structure of the phase designated as $Mn_{1.4}TaO_{3.9}$ (7). The correct composition is $Mn_3Ta_2O_8$, and its tetragonal structure (space group $I4_1/a$ and $a = 11.2728(2)$, $c = 9.3030(3)$ Å) is related to that of fluorite.

Attempts to obtain single crystals at temperatures above 1200°C of the phase denoted "$Mn_{1.4}TaO_{4.2}$" by Turnock (2) led to the discovery of the $Mn_{0.6}Ta_{0.4}O_{1.65}$ phase described in this article. It has a cubic fluorite structure, and its electron diffraction patterns (EDP's) reveal strong diffuse scattering, similar to that found for many other oxygen-deficient oxides with the fluorite structure, including calcium-stabilized zirconia (CSZ) (8), Y_3TaO_7 (9), and $U_{0.2}La_{0.8}O_{1.80}$ (10).

The structural variation of fluorite-related oxides is wide, and it has been extensively investigated for a long time. Stabilized zirconias, e.g., have been much studied in connection with their properties as oxygen ion conductors and their use as solid electrolytes in fuel cells and oxygen sensors (11). A series of fluorite superstructures are found for RE_nO_{2n-2} phases with RE = Ce, Pr, and Tb (12), caused by ordering of oxygen vacancies in concentrations larger than ca. 10%. A vast variety of compounds have structures that can be derived from fluorite, among them the pyrochlore type structure of, e.g., $RE_2Zr_2O_7$ compounds with large RE^{3+} ions (RE = La → ~Gd) (13), $CaHf_4O_9$ and $Ca_6Hf_{19}O_{44}$ (14), and La_3TaO_7 (15). Ordering in defect fluorite MO_{2-x} phases has been discussed by Rossel and Scott (16). Oxygen-deficient oxides with fluorite-related structures also frequently reveal diffuse scattering, observed

[1]To whom correspondence should be sent.

0022-4596/99 $30.00

in single-crystal electron, X-ray, and neutron diffraction studies. The shape of the diffuse scattering is surprisingly similar for chemically different compounds, yet the number of models proposed to explain the phenomenon are almost as many as the number of compounds for which diffuse scattering has been observed.

Although the different models invoked to explain the diffuse scattering are diverse, they can here be formally divided into three categories: (i) models that assume a formation of small regions with an ordered structure, implying a defined ordering of both metal and oxygen atoms in them, (ii) models based on the formation of complexes of oxygen vacancies around certain metal atoms, together with relaxation of metal positions, and (iii) those primarily based on an ordering of oxygen vacancies or oxygen atom displacements.

Microdomains of an ordered phase, coherently intergrown with a cubic fluorite matrix, have been proposed to explain the diffuse scattering for $Ca_xM_{1-x}O_{2-x}$ (M = Zr, Hf and $x = 0.1$–0.2) (17) (domains with the $CaHf_4O_9$ type structure and a diameter of 30 Å), for urania–ceria phases (18) (domains with the pyrochlore type structure, elongated along $\langle 111 \rangle_f$ and with a diameter and axial length of 14 and 28 Å, respectively), for $(U_{1-y}La_y)O_{2-x}$ ($0.7 \leq y \leq 0.8$) (10) (domains of a phase denoted RII), and for the defect fluorites $RE_2Zr_2O_7$ (RE = Gd, Dy, Ho, Er, and Yb) (19) (domains of a pyrochlore phase).

Structural models founded on smaller clusters or local atom-site correlations have been used in the cases of $Ca_{0.15}Zr_{0.85}O_{1.85}$ (20, 21), $Y_{0.39}Zr_{0.61}O_{1.805}$ (22), and Y_3TaO_7 (23). A model based on antiphase domains of ordered oxygen-atom displacements was used by Miida *et al.* (24) to account for the diffuse scattering in CaO-stabilized and Tb_4O_7-stabilized zirconia. The domain size was determined to be 15–20 Å, and the boundaries were proposed to be various planes belonging to the $[111]_f$ zone.

The synthesis and characterization of the cubic fluorite phase $Mn_{0.6}Ta_{0.4}O_{1.65}$ is described below, in particular with regard to a study of the strong diffuse scattering present in its electron diffraction patterns.

EXPERIMENTAL

The compound $Mn_{0.6}Ta_{0.4}O_{1.65}$ was prepared in air by rapid cooling of a melt with the corresponding metal composition from 1400°C. A mixture of $Mn(C_2O_4)$ and Ta_2O_5 was heated in a Pt crucible up to 1450°C, then cooled to 1400°C, and the sample was held at that temperature for 1 h to achieve equilibrium with the surrounding atmosphere. The Pt crucible was then quickly removed from the furnace and rapidly cooled by immersing it in water. The quenched sample had a shiny black color, which turned into dark brown upon grinding.

The metal composition was determined by energy-dispersive X-ray (EDX) analysis, using a LINK AN10000 system mounted in a JEOL JSM-820 scanning-electron microscope. The average of 20 point analyses was used, with the statistical error in each being ca. 1 at.%. The oxygen content was determined by a standard combustion method using a LECO TC444 apparatus.

Phase identification and determination of the unit-cell parameters were carried out using a focusing Guinier–Hägg camera with Cu$K\alpha_1$ radiation and Si as internal standard. The films were evaluated with a film scanner system (25).

A STOE STADI/P diffractometer with Cu$K\alpha_1$ radiation was used for collection of the XRPD data in the 2θ range 20–120° for Rietveld refinements. The sample was placed in symmetrical transmission mode and a linear position-sensitive detector (PSD) covering 4.6° in 2θ was used. The PSD was moved in steps of 0.2°.

Two transmission electron microscopes, a JEOL 2000 FX and a JEOL 3010, were used. The 2000 FX microscope was operated at an acceleration voltage of 200 kV and equipped with a double-tilt holder with $\pm 45°$ limitations. This microscope was primarily used for recording EDP's. The JEOL 3010 microscope is optimized as an HREM instrument with an acceleration voltage of 300 kV, a double-tilt holder with $\pm 20°$ limitations, and an optimal resolution of 1.7 Å. The investigated specimens were crushed and dispersed in butanol and drops of the dispersions were transferred to a holey carbon-coated copper grid.

Thermal analysis measurements were carried out in order to gain information about phase transitions, thermal stability, and changes in the oxygen content. A SETARAM Labsys TG-DTA16 instrument was used for simultaneous thermogravimetric (TG) and differential thermal analysis (DTA) recordings. The measurements were done in air between room temperature and 1550°C, using a heating rate of 5°C/min and sample weights around 200 mg.

A weak-field ac susceptometer (Lake Shore 7130) was used for magnetic measurements in the temperature range 15–300 K, with a magnetic field of 500 A/m^{-1} and a frequency of 500 Hz.

An automated impedance spectrometer (26) was used for conductivity measurements on pressed pellets (porosity 25–30%) furnished with gold electrodes. The pellets were 0.8 cm in diameter and 0.1 cm thick. Data were collected at 200–400°C in the frequency range 10 Hz to 1 MHz.

RESULTS

Phase Analysis and X-Ray Powder Diffraction

Monophasic samples of $Mn_{0.6}Ta_{0.4}O_{1.65}$ were obtained by rapid cooling of a melt from 1400°C. The Guinier–Hägg XRPD pattern showed only eight sharp reflections, which could be indexed by a face-centered cubic unit cell with $a = 4.9826(3)$ Å. Powder patterns from samples quenched

from lower temperatures, 1400 to 1250°C, contained strong fluorite-type reflections together with additional sets of weaker reflections, none of them attributable to known oxides containing Mn and/or Ta. The patterns testify to the presence of a cubic fluorite phase plus several related phases. Similar powder patterns were also obtained for other metal compositions with 50 to 80% Mn. Shifts and splittings of the basic fluorite reflections suggest that a series of fluorite-related phases are formed.

Samples heat treated within the temperature range 1100–1250°C yielded powder patterns that were very similar to each other but showed minor differences in peak positions and in the number of weak reflections present. For temperatures 1100–1150°C, the samples contained minor amounts of Mn_3O_4. The phase(s) formed in this temperature range is probably the one reported by Turnock to be $Mn_{1.4}TaO_{4.2}$ (2). The basic fluorite reflections are split, which implies a symmetry lower than cubic. We have so far been unable to index these patterns, but they demonstrate the existence of several uncharacterized ordered phases, which are presently under investigation. A preliminary ED study has shown that one of them is incommensurately modulated. Samples heat treated below 1100°C contained only $MnTa_2O_6$ and Mn_3O_4.

The metal composition of $Mn_{0.6}Ta_{0.4}O_{1.65}$ was determined by EDX analysis and found to be 60(1) at.% Mn, in agreement with the nominal composition. The stoichiometric compound $Mn_4Ta_2O_9$ (4) was used as a standard. The oxygen content was determined to be 20.1(1) wt.%, which equals the composition $Mn_{0.6}Ta_{0.4}O_{1.65(1)}$. The analysis was checked by a determination of the oxygen content in $Mn_4Ta_2O_9$. The mean oxidation state of Mn is +2.17, which corresponds to ca. 1/6 (or 17%) Mn^{3+}. The formula for the compound may accordingly be written $Mn^{2+}_{0.5}Mn^{3+}_{0.1}Ta_{0.4}O_{1.65}$. The oxygen content is ca. 18% less than for an ideal MO_2 fluorite composition (implying that there are 18% vacancies in the anion array), which is very low. Such low oxygen contents can, however, be found in the literature for other cubic fluorite-type phases, for example $Zr_{0.866}Ca_{0.134}O_{1.7}$, $Zr_{0.786}Y_{0.214}O_{1.7}$ (27), and $Mn_{0.33}Zr_{0.33}Ti_{0.33}O_{1.67}$ (28).

The diffractometer XRPD pattern was used for a Rietveld refinement of $Mn_{0.6}Ta_{0.4}O_{1.65}$, with 10 Bragg peaks for $2\theta < 107°$, using the program GSAS (29). The half-width of the peaks was 0.10° in 2θ at 65°. The metal $M = (Mn_{0.6}Ta_{0.4})$ and O atoms were put in positions 4(*a*) (0,0,0) and 8(*c*) (1/4,1/4,1/4), respectively, in space group *Fm*3*m*. A total number of 11 parameters were refined, yielding $R_F = 3.0\%$ and $S = 1.0$. The fit between observed and calculated patterns is shown in Fig. 1. The refinement verifies that the average X-ray structure of $Mn_{0.6}Ta_{0.4}O_{1.65}$ is that of a cubic fluorite. The isotropically refined displacement parameters, including an absorption contribution, for *M* and O atoms were 2.4(2) and 8(1) Å^2, respectively.

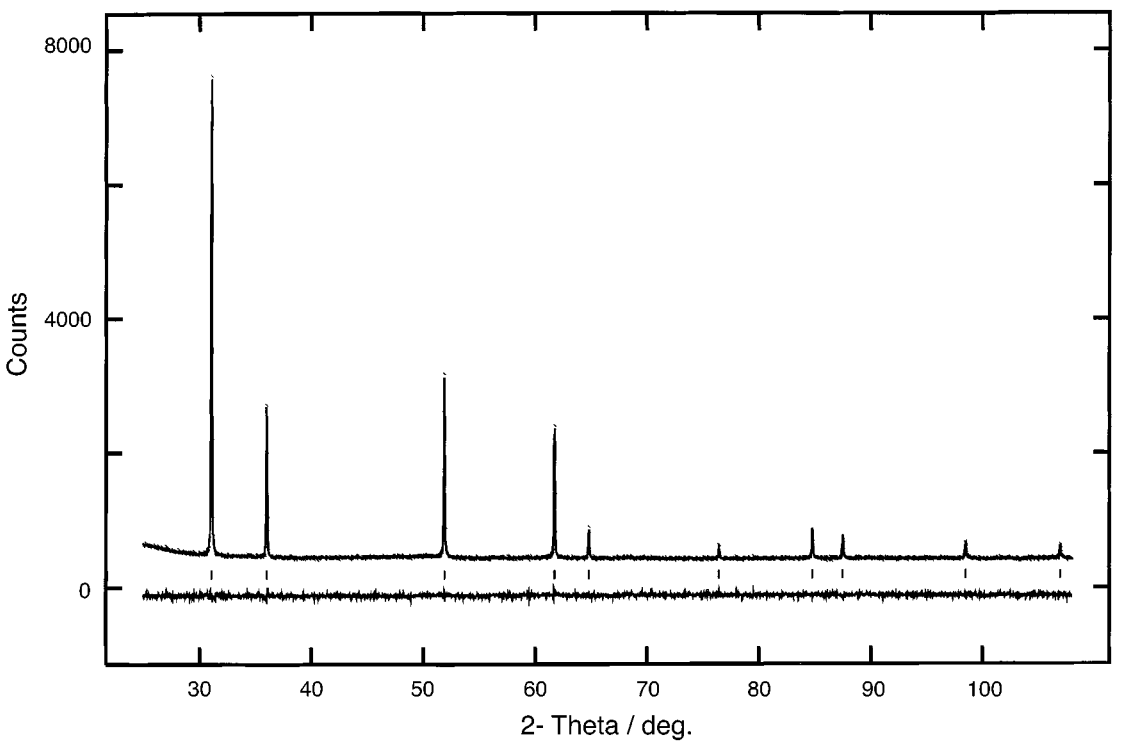

FIG. 1. Observed (points), calculated (solid line), and difference XRPD pattern for $Mn_{0.6}Ta_{0.4}O_{1.65}$.

Thermal Analysis

Simultaneous TG/DTA recordings of $Mn_{0.6}Ta_{0.4}O_{1.65}$ heated in air are shown in Fig. 2. The compound starts to be oxidized and gain weight at 300°C. The oxidation rate is highest around ca. 400°C, and a plateau is reached at 500°C. The oxidation process is exothermal as shown by the DTA curve. The weight gain at 500°C is 1.21 wt%, which corresponds to $Mn^{2+}_{0.3}Mn^{3+}_{0.3}Ta_{0.4}O_{1.75}$, a metal–oxygen composition expected for a compound with, e.g., a pyrochlore-type structure ($A_2B_2O_7 \rightarrow MO_{1.75}$). A small weight loss then takes place between 500 and 750°C, which is small in comparison and agrees with a composition $Mn_{0.6}Ta_{0.4}O_{1.74}$ at 750°C. Guinier–Hägg powder patterns of samples heat-treated for 30 min at 500 and 750°C, respectively, could both be indexed by cubic fluorite-type cells, but with markedly different unit cell parameters, $a = 4.9380(4)$ and 4.9461(2) Å, respectively, compared with that of $Mn_{0.6}Ta_{0.4}O_{1.65}$, $a = 4.9826(3)$ Å. The decrease of the a parameter is primarily associated with the oxidation of some Mn^{2+} to Mn^{3+}, which has a smaller ionic radius. In addition to the cubic fluorite reflections, two broad and very weak, barely discernible, reflections could be observed at positions corresponding to indices $\frac{1}{2} \cdot (111)$ and $\frac{1}{2} \cdot (220)$. It is not certain at this stage whether these reflections are representative for the whole samples, but they may indicate a weak superstructure with a doubled a axis.

The TG curve shows a relatively large weight loss above 750°C, and a plateau at 950°C. A sample heat-treated at 900°C for 30 min and then quenched yielded a powder pattern containing weak and broad peaks of Mn_3O_4, strong and split fluorite reflections, and a number of weaker, but quite sharp reflections indicating that a fluorite-related compound with lower symmetry had been formed. The exact composition of the latter phase is not known, due to the formation of Mn_3O_4, but may still be expected to be close to those of the fluorite phases discussed above.

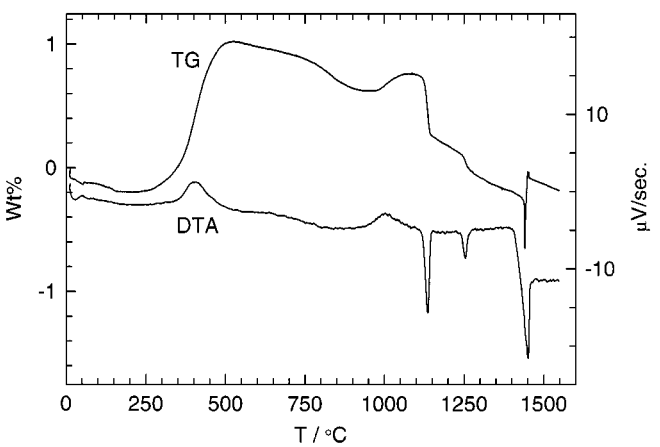

FIG. 2. TG/DTA curves for $Mn_{0.6}Ta_{0.4}O_{1.65}$.

An exothermic DTA peak occurs at 980°C together with a small weight gain which stabilizes at 1050°C, wherupon the TG curve shows no changes up to 1100°C. A sample was fired at 1100°C for 20 min and quenched to room temperature. The powder pattern showed split fluorite-type reflections also in this case, but with the number of reflections and their positions different from the sample heated to 900°C. The powder pattern was found to be quite similar to those of samples fired at 1150–1250°C for longer periods of time.

A very rapid weight loss takes place, together with a sharp endothermal DTA peak, at 1120°C, followed by a slower and continuous weight loss up to 1250°C, where another distinct weight loss and endothermic DTA peak occur. The latter DTA peak is associated with partial melting, as concluded from visual inspection of samples heat treated above 1250°C.

The weight loss then continues at a slower rate up to 1400°C, where the onset of an endothermic DTA peak occurs connected with a melting of the sample. A peculiar jump occurs in the TG curve at 1450°C, during which the weight rapidly first decreases and then increases.

All of the phase transitions and weight changes observed during heating in the temperature range 1000–1550°C were found to be essentially reversible upon cooling.

Magnetic Susceptibility

The inverse of the molar magnetic susceptibility per Mn atom, χ_M^{-1}, for $Mn_{0.6}Ta_{0.4}O_{1.65}$ is shown in Fig. 3 as a function of temperature, T. At higher temperatures a Curie–Weiss law $\chi_M = C/(T + \Theta)$ behavior is approached, indicating an antiferromagnetic interaction between the Mn atoms. At lower temperatures the χ_M^{-1} vs. T graph is curved and shows an increasingly negative deviation from the Curie–Weiss straight line with decreasing temperature. The slope of the approximately linear part of the curve at higher temperatures yields an effective number of Bohr magnetons per Mn atom, $\mu_{\text{eff}} = 5.2(2)$. The expected values for Mn^{2+} and Mn^{3+}, in high-spin states, are 5.9 and ca. 4.9 μ_B, respectively. The observed μ_{eff} value is thus, for reasons obscure, lower than the expected value of ca. 5.8 μ_B, calculated from the composition.

Electrical Conductivity

In order to obtain reproducible data the sample was first cycled a couple of times between 200 and 500°C in air. During the cycling the sample was oxidized and attained the composition $Mn_{0.6}Ta_{0.4}O_{1.75}$ (cf. above), while the conductivity increased by a factor of ca. 10. The impedance was then measured in a cooling–heating–cooling cycle (18 temperatures). The data showed no evidence for any polarization with frequency, e.g., at the electrodes, which strongly suggests that the conductivity is predominantly electronic and that a possible oxygen-ion conductivity accordingly is smaller. The observed capacitance corresponded to a

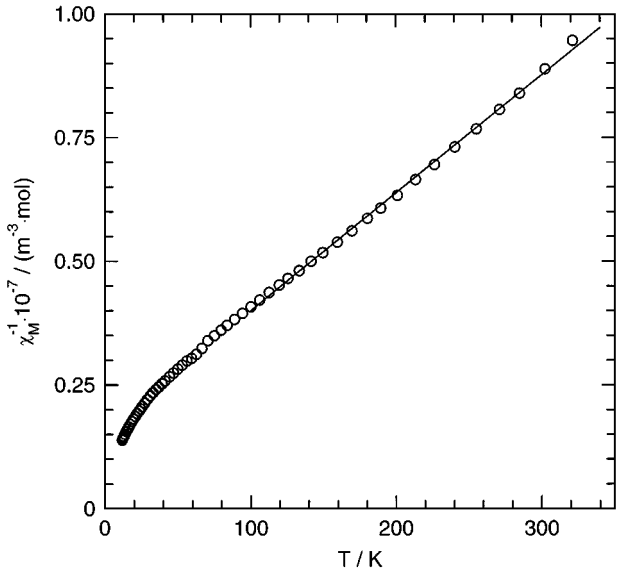

FIG. 3. The inverse of the molar magnetic susceptibility per Mn atom for $Mn_{0.6}Ta_{0.4}O_{1.65}$ versus temperature.

relative dielectric constant of 35. Figure 4 shows a plot of $\log(\sigma)$ vs. $1/T$. The conductivity follows a semiconductor behavior with an activation energy of 0.64 eV. The measurements were made on a compacted powder, and the absolute values of the conductivities are therefore expected to differ from those of a corresponding dense material. Assuming that the intergrain resistances are comparatively small it is however likely that the activation energy is characteristic for a bulk conductivity.

Electron Diffraction

Prominent diffuse scattering was apparent in the EDP's, in addition to the Bragg reflections corresponding to the

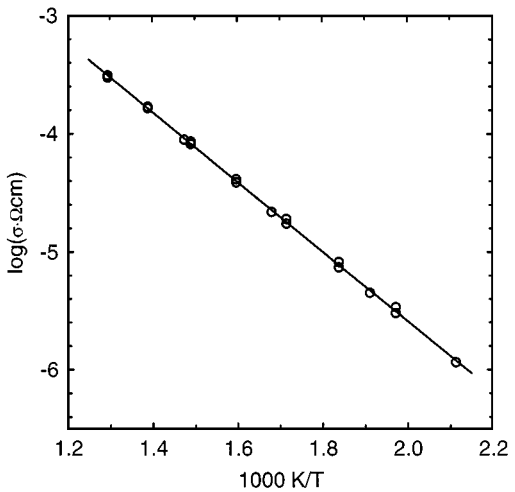

FIG. 4. Conductivity Arrhenius plot for $Mn_{0.6}Ta_{0.4}O_{1.65}$.

*Fm*3*m* fluorite type cell. The shape of the diffuse scattering was found to be almost identical for different crystallites and no evidence for the presence of an amorphous phase could be observed. The symmetry of this diffuse scattering was found to be the same as for the Bragg reflections, **G**, and hence there is no indication that the diffuse scattering decreases the symmetry of the sublattice. EDP's from ten different zones were investigated, with the purpose of determining the three-dimensional shape of the diffuse scattering. The pattern along $\langle 100 \rangle$ exhibited no (or very weak) diffuse scattering, whereas it was prominent in the patterns along other directions. Eight of these are shown in Fig. 5 and described below. Unique reciprocal directions indicated by $[hkl]^*$ are used to describe the positions of the features of the individual EDP's.

$\langle 112 \rangle$. Characteristic rings are observed. The rings have a diameter of $0.1\,\text{Å}^{-1}$ and are centered at $\mathbf{G} + \frac{1}{2}[3\bar{1}\bar{1}]^*$. They are quite sharp and have a roughly homogenous intensity distribution. Another set of diffuse reflections are found around $\mathbf{G} + \frac{1}{2}[11\bar{1}]^*$, separated by a distance of $0.1\,\text{Å}^{-1}$ and somewhat elongated along $[11\bar{1}]^*$. For some crystallites these reflections appeared as slightly concave lines. The center of each of these lines is symmetry-equivalent to the nearest point on an adjacent ring, implying that the reflections are sections of circles lying in other symmetry-equivalent planes. Patterns like these were also obtained for samples quenched from lower temperatures. In some cases the diffuse rings then showed an intensity concentration along $[1\bar{1}0]^*$. Similar rings, in the same position in reciprocal space, have previously been observed for a number of oxygen-deficient fluorite phases, including calcium-stabilized zirconia (8), Y_3TaO_7 (9), and $U_{0.2}La_{0.8}O_{1.80}$ (10).

$\langle 110 \rangle$. Quite sharp and intense diffuse scattering is present. It may be described as pairs of reflections centered at $\mathbf{G} + \frac{1}{2}[1\bar{1}\bar{1}]^*$ and $\mathbf{G} + \frac{1}{2}[1\bar{1}1]^*$, elongated along $[1\bar{1}\bar{1}]^*$ and $[1\bar{1}1]^*$ respectivly, with the distance between the reflections being 0.1 Å. Alternatively, the diffuse scattering can be described as four reflections centered around $\mathbf{G} + [1\bar{1}0]^*$.

$\langle 332 \rangle$. Circles with a diameter of $0.1\,\text{Å}^{-1}$ centered around $\mathbf{G} + \frac{1}{2}[11\bar{3}]^*$ and with an uneven intensity distribution can be seen. In addition, ellipsoid-shaped diffuse scattering is located around $\mathbf{G} + \frac{1}{2}[3\bar{1}\bar{3}]^*$, with axial lengths of 0.1 along $[2\bar{2}0]^*$ and $0.2\,\text{Å}^{-1}$ along $[11\bar{3}]^*$. Another distinct feature of the EDP's in this direction is the diffuse satellites observed at the approximate positions $\mathbf{G} + \langle -0.25, 0.63, -0.60 \rangle^*$ (i.e. $\mathbf{G} \pm (\pm 0.19[11\bar{3}]^* + 0.22[2\bar{2}0]^*)$.

$\langle 114 \rangle$. Two sets of quite sharp and distinct satellite reflections can be observed in this zone. One is positioned at $\mathbf{G} + [0.82, -0.82, 0]^*$ (possibly caused by dynamical scattering) and the other set at $\mathbf{G} + \langle -0.35, -1.25, 0.4 \rangle^*$ (i.e.,

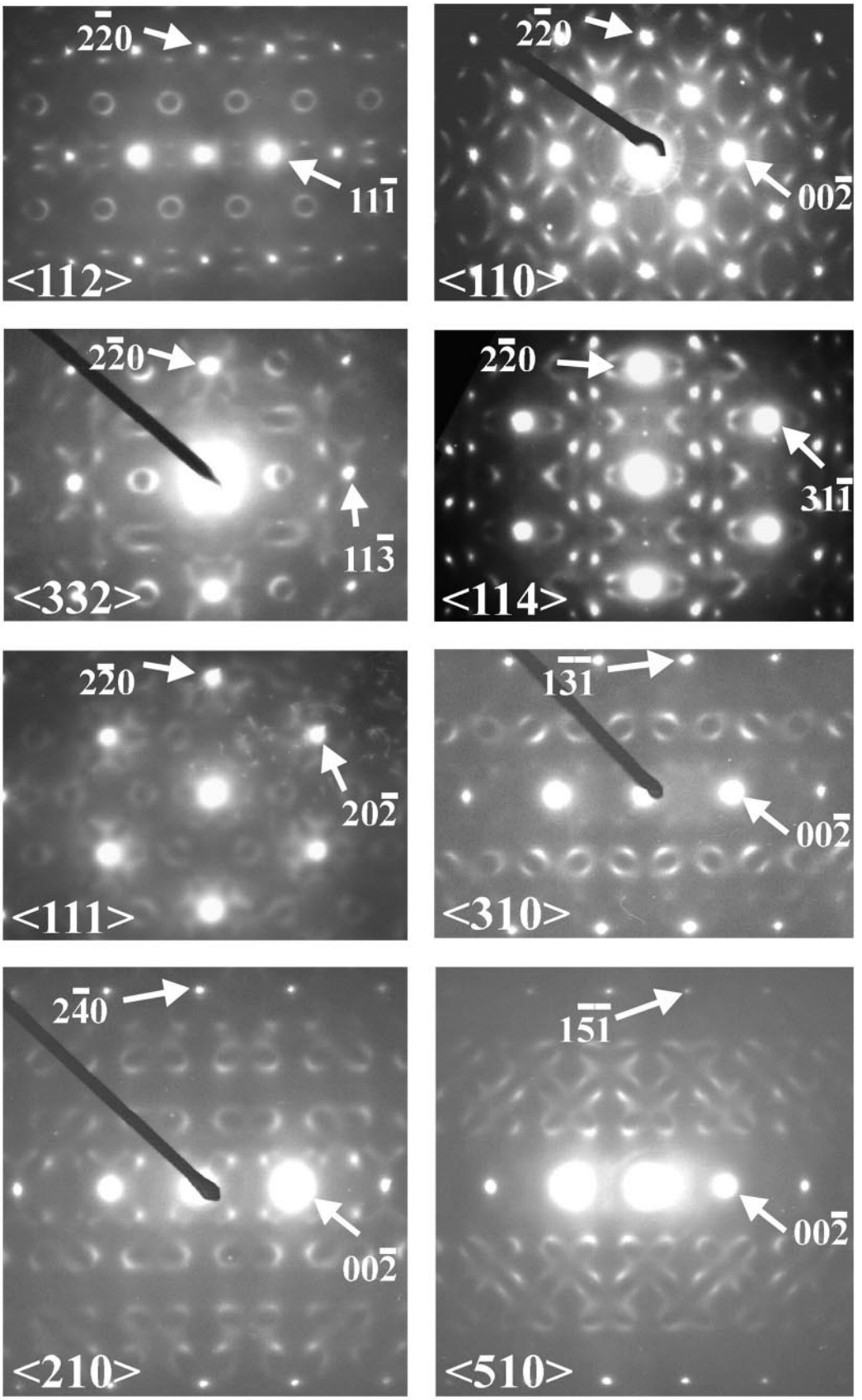

FIG. 5. Electron diffraction patterns for $Mn_{0.6}Ta_{0.4}O_{1.65}$.

$\mathbf{G} \pm (\pm 0.20[44\bar{2}]^* + 0.22[2\bar{2}0]^*)$. Diffuse arcs are further observed at about $\mathbf{G} + 0.29[\bar{2}\bar{2}1]^*$ and $\mathbf{G} + 0.79[\bar{2}\bar{2}1]^*$.

$\langle 111 \rangle$. The diffuse scattering in this zone is moderate but appeared clearly when using longer exposure times. Two sets of diffuse features are present, one set centered around the Bragg reflections, **G**, and the other around $\mathbf{G} + 1/3[4\bar{2}\bar{2}]^*$. The former set has the shape of a six-leaf flower with each leaf centered roughly at $\mathbf{G} + 1/6\langle 422 \rangle^*$ (i.e., $\mathbf{G} \pm 1/6[hkl]^*$, $hkl = 4\bar{2}\bar{2}$, $22\bar{4}$, and $2\bar{4}2$) and extended along the corresponding $\langle 422 \rangle^*$ direction. The latter set has the shape of three circle segments, each directed toward the adjacent Bragg reflections. The circle diameters are $0.1\ \text{Å}^{-1}$ and the center corresponds to 0.17 Å.

$\langle 310 \rangle$. Incomplete diffuse rings are found at $\mathbf{G} + \frac{1}{2}[1\bar{3}1]^*$ and $\mathbf{G} + \frac{1}{2}[1\bar{3}\bar{1}]^*$, with intensity maxima along $[1\bar{3}2]^*$ and $[1\bar{3}\bar{2}]^*$, respectively. The circles have a diameter of $0.2\ \text{Å}^{-1}$.

$\langle 210 \rangle$. Distorted rings are centered approximately at $\mathbf{G} \pm 1/3[2\bar{4}4]^*$. There are also diffuse satellite reflections approximately at $\mathbf{G} \pm 1/6[2\bar{4} \pm 4]^*$.

$\langle 510 \rangle$. The diffuse scattering in this zone appears as a zigzag pattern between the 00*l* row of Bragg reflections and the next row.

The derived three-dimensional shape of the diffuse scattering in reciprocal space is illustrated in Fig. 6. It can be described by hyberbolic cylinders with axes parallel to $\langle 111 \rangle^*$. The diameter and length of the cylinders are ca. 0.1 and $0.5\ \text{Å}^{-1}$, respectively. The intensity of the diffuse scattering on this surface is concentrated in the ring perpendicular to $\langle 111 \rangle^*$ at $\frac{1}{2}\frac{1}{2}\frac{1}{2}$, where the cylinders have their smallest diameter. Slices through the surface, corresponding to the zone axes $\langle 110 \rangle$, $\langle 211 \rangle$, and $\langle 111 \rangle$, are shown in Figs. 7a–7c, for comparison with the observed ED patterns in Fig. 5.

A preliminary ED study of the oxidized phase $Mn_{0.6}Ta_{0.4}O_{1.75}$, obtained by heat treatment of $Mn_{0.6}Ta_{0.4}O_{1.65}$ at 500° in air for 30 min, showed that it exhibits similar diffuse scattering. For some zones, however, e.g., $\langle 111 \rangle$, the diffuse scattering was found to have condensed into sharper reflections. This phase is presently under investigation.

High-Resolution Electron Microscopy

Several zones were examined by high-resolution electron microscopy, including $\langle 100 \rangle$, $\langle 112 \rangle$ and $\langle 110 \rangle$. The $\langle 100 \rangle$ zone was the only one that exhibited a well-ordered structure. All other studied directions revealed different degrees of disorder. Fourier transforms of the HREM images along $\langle 112 \rangle$ and $\langle 110 \rangle$ revealed the same type of diffuse scattering as exhibited by the corresponding diffraction patterns.

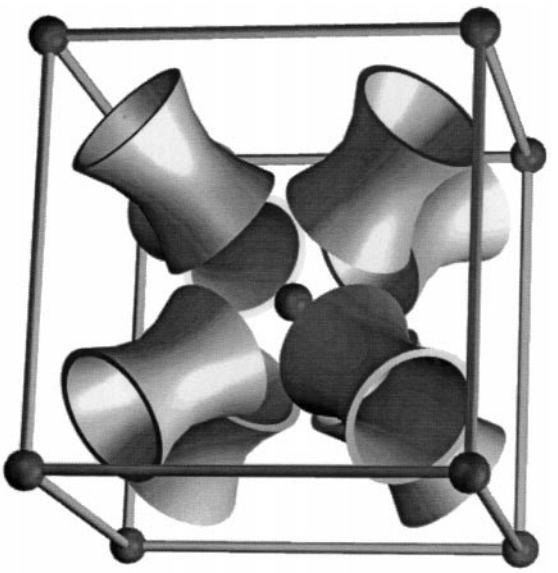

FIG. 6. An illustration of the observed diffuse scattering for $Mn_{0.6}Ta_{0.4}O_{1.65}$ in three-dimensional reciprocal space.

The HREM image along $\langle 100 \rangle$ for the thinner part of the crystal, Fig. 8a, shows a well-ordered pattern, which accords with the absence of diffuse scattering in the corresponding ED pattern. One ordered superstructure domain with an area of ca. 1000 Å^2 was, however, observed, designated by an arrow in Fig. 8a. It can be described by a square unit cell with a parameter $a' = \sqrt{10} \cdot a_f$ parallel with [013]. For the thicker part of the crystal there are some differences in contrast which might originate from clusters of an ordered phase, but the image is difficult to interpret due the crystal thickness.

The image along $\langle 112 \rangle$, Fig. 8b on the other hand, reveals a substantially disordered material. Small domains of a centered superstructure can be discerned, describable by a projected unit cell with $a = 2[11\bar{1}]$ and $b = 2[2\bar{2}0]$. Antiphase boundaries can furthermore be made out for many adjacent domains. An ordered crystal with this structure would give rise to an additional Bragg reflection at $\mathbf{G} \pm \frac{1}{2}[3\bar{1}\bar{1}]^*$, i.e., the center position of the observed diffuse rings in the ED pattern of this zone (cf. Fig. 5a).

The image along $\langle 110 \rangle$, Fig. 8c, shows a relatively ordered structure. Contrast shifts can, however, be observed, particularly along $\langle 111 \rangle$, indicating domains with antiphase boundaries.

The images are admittedly difficult to interpret in view of that they involve averaging along atomic columns but they contain potential and complementary information about the origins of the diffuse scattering. One way to try to extract this information is by Fourier filtering. An image corresponding to that in Fig. 8b and with a simple Fourier filter applied, using the program CRISP (30), is given in

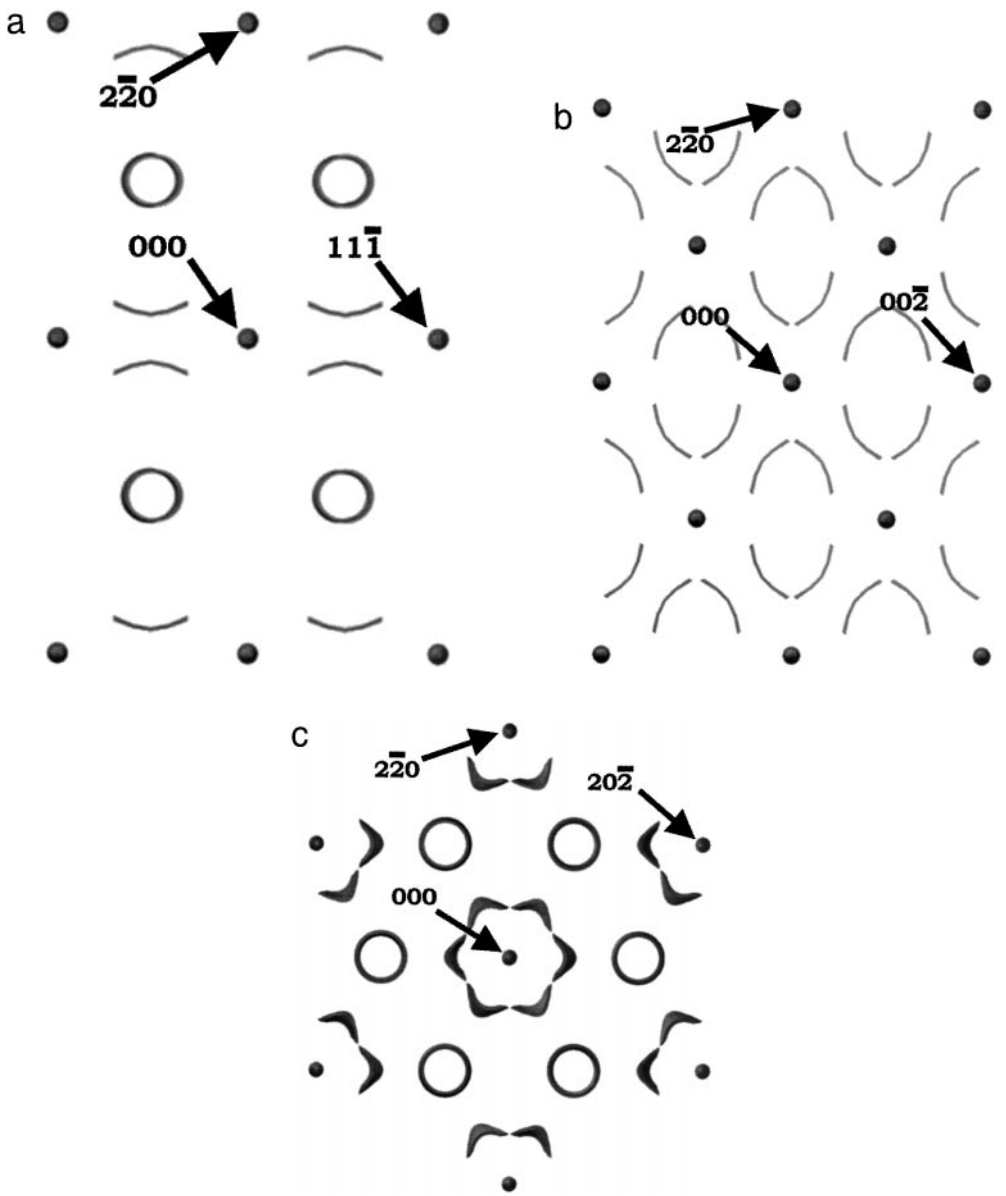

FIG. 7. Sections through the surface shown in Fig. 6 parallel to (a) (110)*, (b) (112)*, and (c) (111)*.

Fig. 8d. The insert shows the Fourier transform of the original scanned image with the areas used for the reverse transform encircled. The larger circles enclose regions where pronounced diffuse rings are observed in the corresponding EDP. Although the filtered image can be expected to contain artifacts introduced by the applied filter it appears to demonstrate the presence of 10–20 Å large domains with a centered superstructure.

A Structural Model for Local Metal Ordering

The observed diffuse scattering may quite generally be stated to originate from a local order of metal and/or oxygen atoms and their displacements from the average structure. While it is recognized that these components accompany each other, we believe that the diffuse scattering in the present case can be principally ascribed to an ordering of metal atoms for the following reasons: The Mn and Ta atoms have very different atomic numbers, and microdomains with ordered metal arrangements should thus show a high contrast in HREM images for some directions, as experimentally observed. It can be remarked here that much smaller atomic number differences for metal atoms are found in most of the fluorite phases that have been investigated for diffuse scattering, although Miida et al. (31) observed a clear metal ion ordering along $\langle 111 \rangle$ in defect

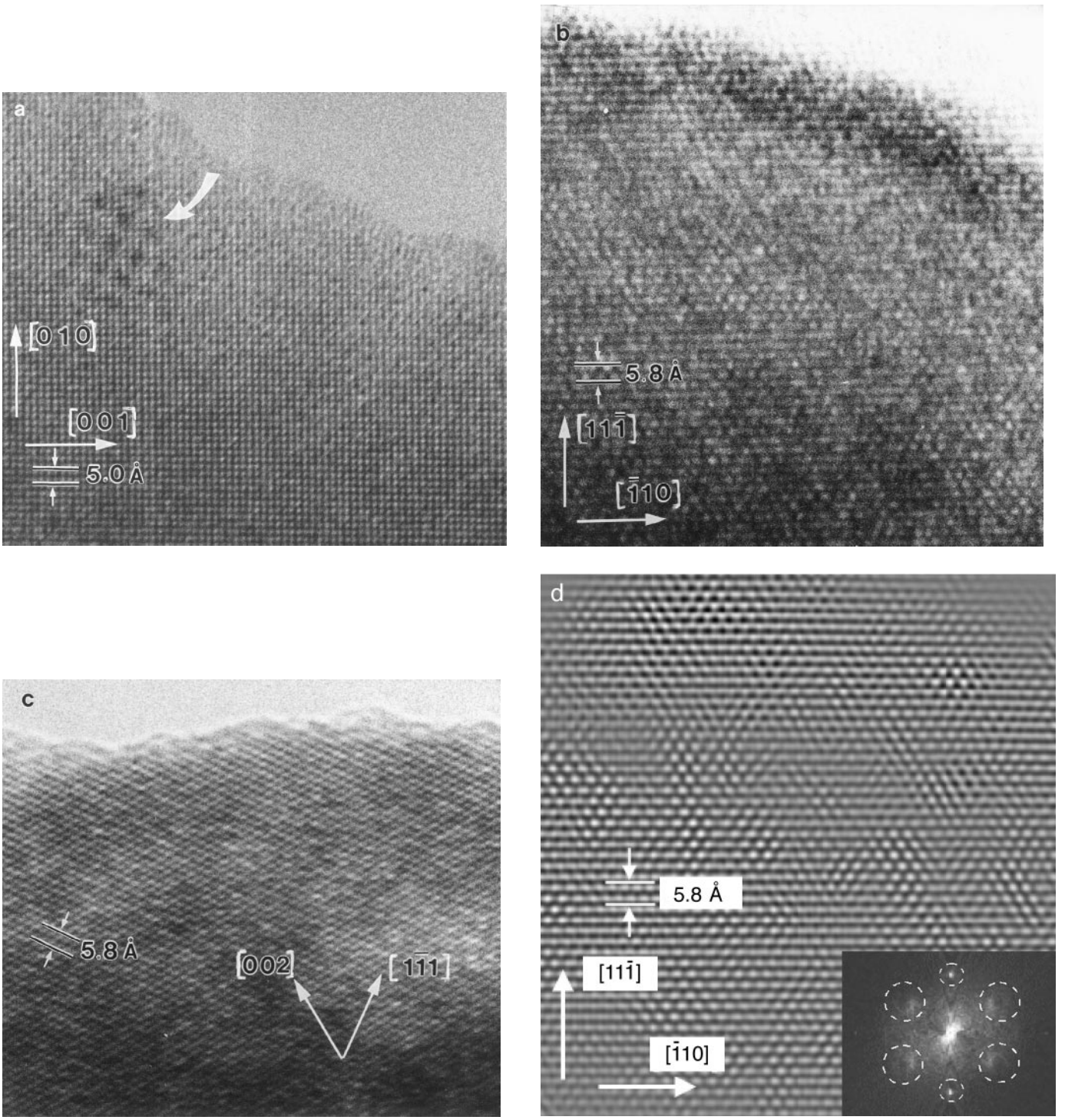

FIG. 8. HREM images of $Mn_{0.6}Ta_{0.4}O_{1.65}$ (a) along [100], (b) [112], (c) [110], and (d) the image in (b) with a Fourier filter applied.

fluorite-type $(Y_2O_3)_{1-x}(Nb_2O_5)_x$ $(0.21 \leq x \leq 0.2)$ solid solutions. This scattering is furthermore found to be essentially preserved for the phase oxidized at 500°C, which should have an oxygen atom arrangement substantially more changed than that of the metal atoms.

Different two-dimensional models were tested, consisting of domains of a heavy-atom superstructure on the $\langle 112 \rangle$ and $\langle 110 \rangle$ projections of a fluorite structure. The Fourier transforms of the models were computed and compared with the observed EDP's. The simulations were made "by

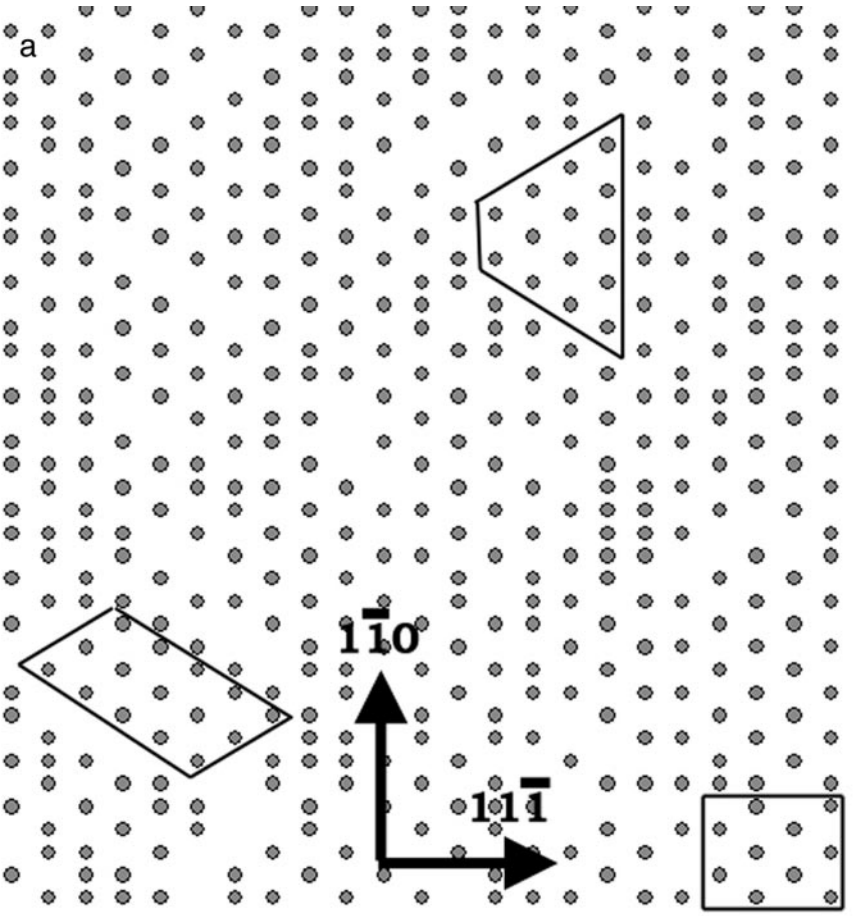

FIG. 9. (a) A two-dimensional metal-atom model for the observed diffuse scattering from $Mn_{0.6}Ta_{0.4}O_{1.65}$ in the $\langle 112 \rangle$ zone and (b) the corresponding Fourier transform.

hand" and primarily aimed at deriving a model that could account for the diffuse rings around $\mathbf{G} \pm \frac{1}{2}[3\bar{1}\bar{1}]^*$ in the $\langle 112 \rangle$ zone. A two-dimensional centered superstructure with unit-cell parameters $a = 2[11\bar{1}]$ and $b = 2[2\bar{2}0]$ was used in the simulations, such as observed experimentally in the $\langle 112 \rangle$ HREM image. An extended superstructure of this kind can be noted to produce a Bragg reflection at $\mathbf{G} \pm \frac{1}{2}[3\bar{1}\bar{1}]^*$, i.e., at the center of the diffuse rings. The best agreement with the observed diffuse scattering was obtained for an average domain size of ca. 10 Å, and with antiphase boundaries between adjacent domains, distributed in different directions. It was furthermore found advantageous to use a narrow distribution of the domain size, and thus on the average a relatively uniform spacing between the domains, implying that there are in the model correlations between site occupancies over comparatively large distancies. This model and its Fourier transform (FT) are illustrated in Figs. 9a and 9b, respectively. The FT shows a clear circular intensity distribution around $\mathbf{G} \pm \frac{1}{2}[3\bar{1}\bar{1}]^*$ and agrees well with the corresponding observed ED pattern in Fig. 5. The additional diffuse reflections around $\mathbf{G} \pm \frac{1}{2}[11\bar{1}]^*$ in the experimental pattern are sections of the same type of rings positioned in other symmetry-related directions, and they may thus be assumed to be generated by a model extended to three dimensions.

A similar model for the $\langle 110 \rangle$ direction is shown in Fig. 10. The ordered domains have an approximate diameter of 10 Å, and antiphase modulations are applied in the $\langle 111 \rangle$ directions. The FT shows pairs of diffuse reflections around $\mathbf{G} \pm \frac{1}{2}[1\bar{1}\bar{1}]^*$, similar to those in the experimental ED pattern in Fig. 5.

In addition, reverse Monte Carlo calculations were carried out, using the program DISCUS-3.0 (32) and digitalized ED patterns. The Mn and Ta atoms in these calculations were initially randomly distributed on a 100×100 two-dimensional rectangular lattice, corresponding to a $\langle 112 \rangle$ projection of the fluorite lattice, and randomly chosen Mn–Ta atom pairs were then allowed to switch positions. The obtained simulated structure agreed essentially with that simulated "by hand," particularly in that it contained small regions of a centered superstructure, but had a more random appearance, as could be expected.

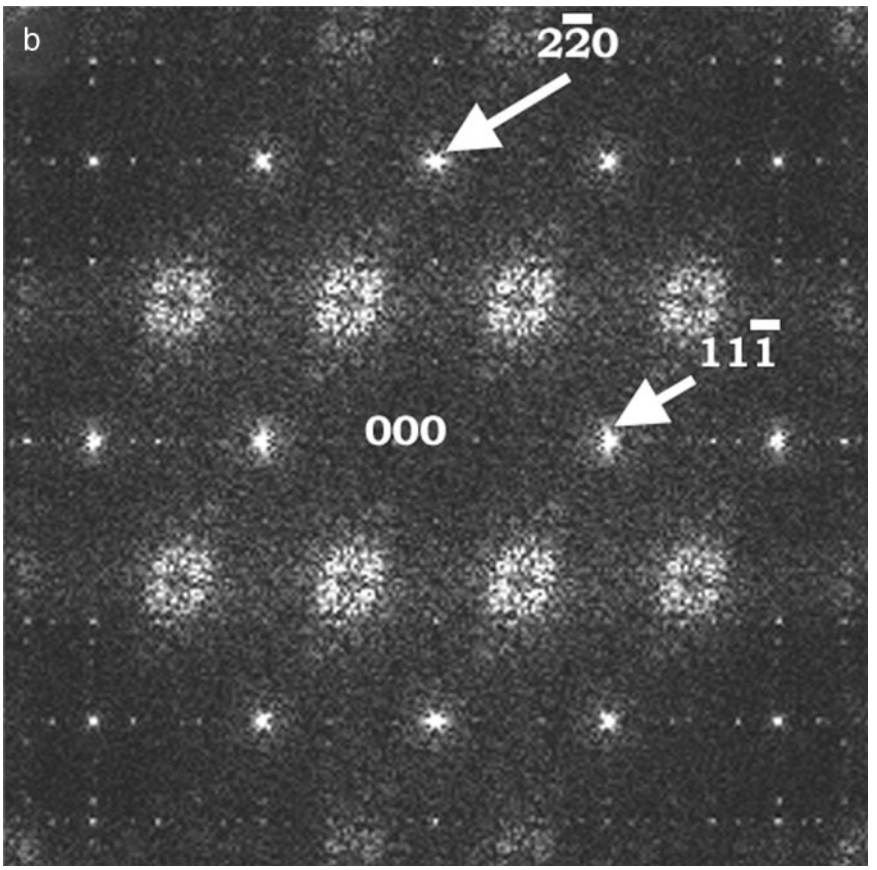

FIGURE 9—*Continued*

DISCUSSION

The diffuse scattering observed for $Mn_{0.6}Ta_{0.4}O_{1.65}$ shows similarities to that yielded by many cubic fluorite phases, and it is practically identical to that observed for $U_{0.2}La_{0.8}O_{1.80}$ (10), La_3TaO_7 (15) and urania–ceria phases (18). For these phases the diffuse scattering has been attributed to microdomains of, respectively, a hexagonal RII phase, a fluorite-related phase with an undetermined structure and a pyrochlore phase.

For $Mn_{0.6}Ta_{0.4}O_{1.65}$ we regard it as likely, for the reasons given above, that the diffuse scattering is primarily associated with an ordering of metal atoms and less with an accompanying ordering of oxygen atom vacancies and atom displacements. A quantitative model that could separate out different contributions would probably require single-crystal diffraction data. The diffuse scattering is reasonably well accounted for in two dimensions, in the zones $\langle 112 \rangle$ and $\langle 110 \rangle$, by ca. 10 Å large domains of a metal atom superstructure and antiphase boundaries between adjacent domains.

The actual microdomain structure may be one of a known structure type. One such structure that appears to agree with the present data, at least partly, is the cubic $A_2B_2O_7$ pyrochlore type (13), which has a unit-cell parameter twice that of the fluorite structure. A $\langle 100 \rangle$ projection of the pyrochlore structure shows no metal ordering, which accords with the absence of any evidence for order in the experimental HREM image in Fig. 8a. Projections of the pyrochlore structure in other directions, including $\langle 112 \rangle$ and $\langle 110 \rangle$, however, shows columns of metal atoms with unequal proportions of A and B atoms, corresponding to the type of centered two-dimensional superstructure described above.

The $Mn_{0.6}Ta_{0.4}O_{1.65}$ phase contains both Mn^{2+} and Mn^{3+}, and its formula can be written as $Mn^{2+}_{0.5}Mn^{3+}_{0.1}Ta_{0.4}O_{1.65}$. The Shannon–Prewitt ionic radii (33) for six-coordinated Mn^{2+}, Mn^{3+}, and Ta^{5+} are 0.83, 0.65, and 0.64 Å, respectively. The radii of Mn^{3+} and Ta^{5+} are very similar, and these ions are therefore more likely to be able to occupy a position in a crystal structure in a random statistical way, in comparison with the larger Mn^{2+} ion. A pyrochlore formula for $Mn_{0.6}Ta_{0.4}O_{1.65}$ may accordingly be written as $Mn^{2+}_2(Mn^{3+}_{0.4}Ta_{1.6})O_{6.6}$. A hypothetical pyrochlore structure with this composition would contain octahedrally coordinated Mn^{3+} and Ta^{5+} ions, the larger

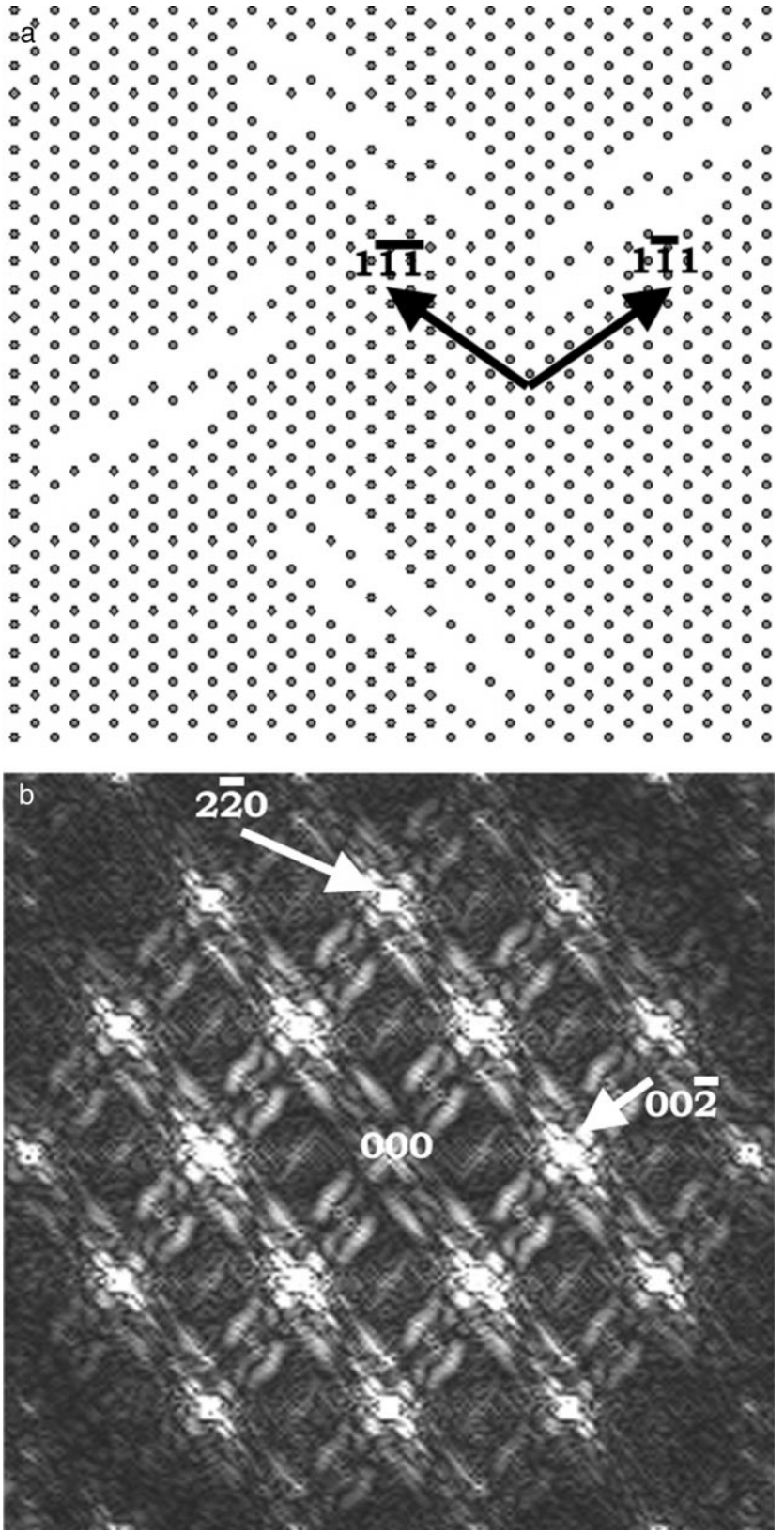

FIG. 10. (a) A two-dimensional metal-atom model for the observed diffuse scattering from $Mn_{0.6}Ta_{0.4}O_{1.65}$ in the $\langle 110 \rangle$ zone and (b) the corresponding Fourier transform.

Mn^{2+} ions coordinated by six oxygen atom forming a puckered hexagon and two further oxygen atoms at the 8(*b*) positions, the latter having a fractional occupancy of 60%. The A/B ionic radius ratio for this structure is ≈ 1.24, which is above the minimum value of 1.2 found to be required for $RE_2M_2O_7$ (M = Zr, Ti) to adopt the pyrochlore structure (34). It should be remarked here, however, that a pyrochlore $Mn_2Ta_2O_7$ has not been prepared, whereas the Mn^{2+}-containing compound $Mn_2Sb_2O_7$, with the larger A/B ionic radius ratio 1.31, does form (35).

The defect fluorite type compounds $RE_2Zr_2O_7$ (RE = Gd, Tb, Dy, Ho, Er, and Yb) have been studied by Komyoji *et al.* (19) using the EXAFS technique, and these authors concluded that the materials contain microdomains with pyrochlore structures. The A/B ionic radius ratio for these phases varies between 1.17 and 1.26. These compounds were further studied by Withers *et al.* (36), by electron diffraction, and show diffuse scattering similar to that described here for $Mn_{0.6}Ta_{0.4}O_{1.65}$.

When $Mn_{0.6}Ta_{0.4}O_{1.65}$ is oxidized in air it attains a stable metal/oxygen ratio of 1.75, the usual metal/oxygen ratio found for pyrochlores. Preliminary ED studies of the oxidized phase shows that it exhibits mainly the same type of diffuse scattering as $Mn_{0.6}Ta_{0.4}O_{1.65}$. The oxidized phase contains a larger fraction of Mn^{3+} ions and accordingly has a smaller unit-cell parameter. The A/B ionic radius ratio for a pyrochlore structure with this composition is also smaller, ≈ 1.15, which should destabilize the structure. The oxidation occurs, however, at low temperatures and the metal atom arrangement may therefore be assumed to remain unchanged.

ACKNOWLEDGMENTS

The authors thank Dr. T. Hörlin for help with the conductivity measurements and Professor M. Nygren for support and valuable discussions. This work has been financially supported by the Swedish Natural Science Foundation.

REFERENCES

1. J. Grins, P.-O. Käll, and G. Svensson, *J. Solid State Chem.* **117,** 48 (1995).
2. A. C. Turnock, *J. Amer. Ceram. Soc.* **49,** 382 (1966).
3. H. Weitzel, *Z. Kristallogr.* **144,** 238 (1976).
4. F. Bertaut, L. Corliss, F. Forrat, R. Aleonard, and R. Pauthenet, *Phys. Chem. Solids* **21,** 234 (1961).
5. N. Schönberg, *Acta Metallurgica* **3,** 14 (1955).
6. J. Grins and A. Tyutyunnik, *J. Solid State Chem.* **137,** 276 (1998).
7. S. Esmaeilzadeh, J. Grins, and A. Fitch, *J. Mater. Chem.* **8,** 2493 (1998).
8. B. Hudson and P. T. Mosely, *J. Solid State Chem.* **19,** 383 (1976).
9. J. G. Allpress and H. J. Rossel, *J. Solid State Chem.* **27,** 105 (1979).
10. P. Garcia-Chain, R. M. Rojas, P. Herrero, and J. R. Günther, *J. Solid State Chem.* **108,** 236 (1994).
11. O. T. Sørensen (Ed.), "Nonstoichiometric Oxides." Academic Press, New York, 1981.
12. P. Kunzmann and L. Eyring, *J. Solid State Chem.* **14,** 229 (1975).
13. M. A. Subramanian, G. Aravamudan, and G. V. Subba Rao, *Prog. Solid State Chem.* **15,** 55 (1983).
14. J. G. Allpress, H. J. Rossel, and H. G. Scott, *J. Solid State Chem.* **14,** 264 (1975).
15. H. J. Rossel, *J. Solid State Chem.* **27,** 115 (1979).
16. H. J. Rossel and H. G. Scott, *J. Phys. Colloq*, **38**(C7), 28 (1977).
17. J. G. Allpress and H. J. Rossel, *J. Solid State Chem.* **15,** 68 (1975).
18. M. C. Pienkowski, M. L. Jenkins, and P. T. Moseley, *J. Solid State Chem.* **92,** 543 (1991).
19. D. Komyoji, A. Yoshiasa, T. Moriga, S. Emura, F. Kanamaru, and K. Koto, *Solid State Ionics* **50,** 291 (1992).
20. R. B. Neder, F. Frey, and H. Schulz, *Acta. Crystallogr. Sect. A* **46,** 799 (1990).
21. M. Morinaga and J. B. Cohen, *Acta Crystallogr. Sect A* **36,** 520 (1980).
22. T. R. Welberry, R. L. Withers, J. G. Thompson, and B. D. Butler, *J. Solid State Chem.* **92,** 543 (1991).
23. T. Tanaka, N. Ishizawa, M. Yoshimura, F. Marumo, and H. Oyanagi, *J. Solid State Chem.* **114,** 79 (1995).
24. R. Miida, M. Tanaka, H. Arashi, and M. Ishigame, *J. Appl. Crystallogr.* **27,** 67 (1994).
25. K. E. Johansson, T. Palm, and P.-E. Werner, *J. Phys. E* **13,** 1289 (1980).
26. T. Hörlin, *Chemica Scripta* **25,** 270 (1985).
27. M. Morinaga and J. B. Cohen, *Acta Crystallogr. Sect. B* **35,** 789 (1979).
28. G. Bayer, *J. Amer. Ceram. Soc.* **53,** 294 (1976).
29. A. C. Larson and R. B. Dreele, Los Alamos National Laboratory Report No LA-UR-86-748 (1987).
30. S. Hovmöller, *Ultramicroscopy* **41,** 121 (1992).
31. R. Miida, F. Sato, M. Tanaka, H. Naito, and H. Arashi, *J. Appl. Crystallogr.* **30,** 272 (1997).
32. TH. Proffen and R. B. Neder, *J. Appl. Crystallogr.* **30,** 171 (1997).
33. R. D. Shannon, *Acta Crystallogr. Sect. A* **32,** 751 (1976).
34. R. Collongues, F. Queyroux, M. Perez Y Jorba, and J.-C. Gilles, *Bull. Soc. Chim. France* 1141 (1961).
35. F. Brisse, D. J. Stewart, V. Sejdl, and O. Knop, *Can. J. Chem.* **50,** 3648 (1972).
36. R. L. Withers, J. G. Thompson, and P. J. Barlow, *J. Solid State Chem.* **94,** 105 (1991).